Diffraction theory of nanotwin superlattices with low symmetry phase: Application to rhombohedral nanotwins and monoclinic M_A and M_B phases

Yu U. Wang*

Department of Materials Science and Engineering, Virginia Tech, Blacksburg, Virginia 24061, USA
(Received 31 May 2007; published 17 July 2007)

The Brillouin zone-dependent conditions for coherent and adaptive diffractions are formulated. Adaptive diffraction phenomenon of nanotwins is analyzed. Extraordinary Bragg reflection peaks appear and adaptively shift along the conventional twin peak splitting vectors, whose positions are determined by lever rule according to twin variant volume fractions. Analysis of rhombohedral nanotwins shows that the nanotwin superlattices of rhombohedral phase with {001} and {110} twin planes diffract incident waves just like monoclinic M_A and M_B phases, respectively, whose lattice parameters are intrinsically related to that of rhombohedral phase. Crystallographic analysis of rhombohedral nanotwins by nanodomain averaging gives the same monoclinic M_A and M_B phases.

I. INTRODUCTION

A diffraction theory of nanotwin superlattices with low symmetry phases was recently developed.[1] The theory reveals peculiar diffraction phenomena due to the coherent scattering from nanodomained microstructures that cannot be explained by conventional diffraction theory of coarse-domained materials. It predicts an adaptive diffraction behavior, where extraordinary Bragg reflection peaks appear at reciprocal superlattice sites in the immediate vicinity of fundamental reflection spots of the constituent crystals and adaptively shift along the twin peak splitting vectors, whose positions are determined by lever rule according to twin variant volume fractions.[1] A conventional interpretation of the new peaks would lead to erroneous assignment of new phases. As an application example, nanotwin superlattice of tetragonal phase has been analyzed in detail,[1] which shows that diffraction perceives (101) tetragonal nanotwins as monoclinic (M_C-type) phase, where the monoclinic lattice parameters a_m, b_m, and c_m measured from (H00), ($0K$0) and ($00L$) reflection spots, respectively, are intrinsically related to the lattice parameters a_t and c_t of tetragonal phase as follows:[1]

$$a_m = \omega a_t + (1 - \omega)c_t, \quad b_m = a_t, \quad c_m = \omega c_t + (1 - \omega)a_t,$$

(1)

where ω is the twin variant volume fraction of tetragonal phase. These intrinsic lattice parameter relationships between monoclinic M_C and tetragonal phases are confirmed by extensive diffraction data reported in the literature over wide ranges of temperature, composition, and electric field in ferroelectric $Pb[(Mg_{1/3}Nb_{2/3})_{1-x}Ti_x]O_3$ (PMN-PT) and $Pb[(Zn_{1/3}Nb_{2/3})_{1-x}Ti_x]O_3$ (PZN-PT).[2] The same relationships are obtained from crystallographic analysis of tetragonal twins by domain averaging.[2,3] Recently, nanotwins of tetragonal phase with domain size about 10 nm has been directly observed by transmission electron microscopy (TEM) combined with convergent beam electron diffraction (CBED) in PMN-PT,[4] which appears to be monoclinic M_C phase in diffraction and polarized light microscopy. The peculiar nanot-

win diffraction phenomenon and, in particular, lack of taking into account the coherent scattering and interference effects of nanodomained microstructures led to misinterpretation of diffraction data and identification of erroneous (monoclinic) phase.

To date, three types of monoclinic phases (M_A, M_B, and M_C) have been reported based on high-resolution x-ray and neutron diffractions.[5] Following the discovery of monoclinic M_A phase around the morphotropic phase boundary (MPB) in ferroelectric $Pb(Zr_{1-x}Ti_x)O_3$ (PZT) by high-resolution synchrotron x-ray powder diffraction,[6] x-ray and neutron diffraction experiments also discovered M_A, M_B, and M_C phases around the MPBs in ferroelectric PMN-PT and PZN-PT, depending on composition as well as thermal and electric histories.[5] As will be shown in this paper, similar intrinsic relationships between M_A and M_B phases and rhombohedral nanotwins exist, as in the case of M_C phase and tetragonal nanotwins discussed above. It is worth noting that there are only three types of crystallographic nanotwins in these MPB-based ferroelectric perovskite-type solid solutions, namely, rhombohedral twins of {001} and {110} twin planes and tetragonal twins of {101} twin planes, which correspond to M_A, M_B, and M_C phases, respectively; furthermore, in experiments M_A and M_B phases are always observed to be associated with rhombohedral phase, while M_C phase is always observed to be associated with tetragonal phase. Very recently, complementary TEM, CBED, electron paramagnetic resonance, and high-resolution synchrotron x-ray diffraction experiments observe, instead of monoclinic phase, the formation of nanodomains of tetragonal and rhombohedral phases in PZT around its MPB;[7] more importantly, the experiments establish direct correlation between the formation of nanodomains and the appearance of extraordinary peak profiles in x-ray powder diffraction,[7] which is previously linked to a monoclinic phase. Clearly, nanoscale domain microstructures play a crucial role in correct interpretation of diffraction data and identification of phases. In order to better understand experimental observations, detailed analysis of coherent scattering and interference of nanodomains is required. In this paper, we report diffraction and crystallographic analyses of rhombohedral nanotwins, which has par-

ticular relevance to the diffraction observation of M_A and M_B phases in MPB-based ferroelectric perovskites. This work complements the previous analysis of tetragonal nanotwins with relevance to M_C phase.[1,2]

In this paper, we first discuss the peculiar behaviors of nanotwin diffraction as compared to the conventional diffraction phenomenon of coarse-domained materials. Then we apply the general nanotwin diffraction theory to the special cases of {001} and {110} rhombohedral nanotwins. We also present crystallographic analysis of rhombohedral nanotwins by performing nanodomain averaging, which gives the same conclusions as from diffraction analysis.

II. ADAPTIVE DIFFRACTION PHENOMENON OF NANOTWINS

In nanodomained materials, the domain sizes are much smaller than the coherence length of diffraction radiation, thus scattered waves from individual nanodomains coherently superimpose in diffraction. For a one-dimensional nanotwin superlattice, i.e., the dimensions of coherent scattering volume are much larger than the nanoscale twin layer thickness, the Fourier transform of the electron density distribution $n(\mathbf{r})$ in the superlattice is[1]

$$\tilde{n}(\mathbf{k}) = \frac{1}{VT} \sum_{\mathbf{K}^{(1)}} \sum_{\kappa^{(s)}} g(\kappa^{(s)}, \mathbf{K}^{(1)}) \delta(k_x - K_x^{(1)} - \kappa^{(s)})$$
$$\times \delta(k_y - K_y^{(1)}) \delta(k_z - K_z^{(1)}), \quad (2)$$

where

$$g(\kappa^{(s)}, \mathbf{K}^{(1)}) = \tilde{n}_1^0(\mathbf{K}^{(1)}) f_1(\kappa^{(s)}) + \tilde{n}_2^0(\mathbf{K}^{(1)} + \Delta\mathbf{K}^{(1)}) f_2(\kappa^{(s)} + \gamma\mathbf{s} \cdot \mathbf{K}^{(1)}), \quad (3)$$

$$\kappa^{(s)} = \frac{2\pi s - \mathbf{L} \cdot \mathbf{K}^{(1)}}{\mathbf{L} \cdot \boldsymbol{\tau}}, \quad (4)$$

$$f_1(\kappa) = \frac{2}{\kappa} \sin\frac{\kappa T_1}{2} e^{i(\kappa T_1/2)}, \quad f_2(\kappa) = \frac{2}{\kappa} \sin\frac{\kappa T_2}{2} e^{-i(\kappa T_2/2)}, \quad (5)$$

$T = T_1 + T_2 = \mathbf{L} \cdot \boldsymbol{\tau}$ is the thickness of the twinned bilayer structural basis, T_1 and T_2 are the respective thicknesses of the twin layers, $\mathbf{L}$ is the primitive lattice translation vector of the nanotwin superlattice, $\boldsymbol{\tau}$ and $\mathbf{s}$ are unit vectors normal to the twin plane and along the twinning shear direction, respectively, γ is the magnitude of twinning shear strain, V is the primitive cell volume of the constituent crystal, $\tilde{n}_1^0(\mathbf{k})$ and $\tilde{n}_2^0(\mathbf{k})$ are the structure factors of respective twin layer crystals [a tilde (~) above a function indicates its Fourier transform], $\delta(k)$ is Dirac delta function, s indicates all possible integers, $\mathbf{K}^{(1)}$ collectively represent all reciprocal lattice sites of one twin layer crystal, and

$$\Delta\mathbf{K}^{(1)} = -(\gamma\mathbf{s} \cdot \mathbf{K}^{(1)})\boldsymbol{\tau} \quad (6)$$

represents the corresponding Bragg twin peak splitting vectors due to twinning deformation. The unit vectors $\boldsymbol{\tau}$ and $\mathbf{s}$

are perpendicular to each other and have been chosen as x and z axes, respectively, and used in Eq. (2) for convenience.

The coherent diffraction of nanotwin superlattices, as described by Eqs. (2)–(6), exhibits some peculiar general behaviors worthy of further discussions. Before applying the general theory to the special case of rhombohedral nanotwins, we discuss nanotwin diffraction in comparison to coarse-domain diffraction and the conditions for transitions from coherent and adaptive diffractions to conventional diffraction.

(i) *Twin peak splitting*. The twin peaks, as correlated by vector $\Delta\mathbf{K}^{(1)}$ given in Eq. (6), split in the twin plane normal direction defined by unit vector $\boldsymbol{\tau}$, and is Brillouin zone dependent through the fundamental reciprocal lattice vector $\mathbf{K}^{(1)}$ of the constituent crystal. The splitting vector $\Delta\mathbf{K}^{(1)}$ is proportional to the twin shear strain magnitude γ, and depends on the projection (within a minus sign) of fundamental reciprocal lattice vector $\mathbf{K}^{(1)}$ onto the twin shear direction defined by unit vector $\mathbf{s}$. This twin peak splitting phenomenon is observed in conventional diffraction of coarse-domained materials, which is characteristic of structural twins.

(ii) *Peak broadening*. The fundamental peaks broaden due to the finite thickness of twin layers. The broadening is in the twin plane normal direction $\boldsymbol{\tau}$ along the twin peak splitting vector $\Delta\mathbf{K}^{(1)}$. The functions $f_1(\kappa)$ and $f_2(\kappa)$ defined in Eq. (5) describe the broadened profiles and phase angles of fundamental twin peaks. This peak broadening phenomenon is also observed in conventional diffraction of coarse-domained materials, which allows an estimation of domain sizes from peak broadness.

(iii) *Coherent scattering and interference effects*. For coarse-domained materials, domain sizes are comparable to or larger than the coherence length of diffraction radiation, thus scattered waves from individual domains form reflection peaks independently without interference, which gives the conventional diffraction phenomena, as illustrated in Fig. 1(a) for coarse twins and discussed above in (i) and (ii). When the domain sizes are significantly smaller than the coherence length of diffraction radiation, i.e., nanoscale domains or nanodomains, scattered waves from individual nanodomains coherently superimpose to form Bragg reflection peaks, where constructive (in-phase) and destructive (out-of-phase) interferences lead to significant change in peak intensity profiles. In the case of twin-related nanodomains, new adaptive Bragg reflection peaks appear while the conventional Bragg peaks disappear, as illustrated in Fig. 1(b). Such peculiar diffraction phenomena produced by coherent scattering and interference effects of nanodomains cannot be explained by conventional diffraction theory of coarse-domained materials. There is a transition between peculiar diffraction of nanotwins and conventional diffraction of coarse domains, where the transition condition depends on domain size, twinning shear strain magnitude, and Brillouin zones, as will be discussed in the following. When nanodomains coexist with coarse domains, the peak profiles are incoherent summation of the new adaptive peaks and the conventional peaks, because the distances between coarse domains and sets of nanodomains exceed the coherence length, resulting in loss of interference. The resultant peak
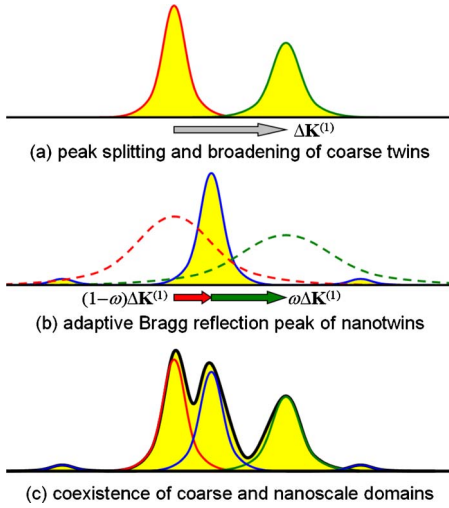
FIG. 1. (Color online) Schematic illustrations of diffraction phenomena of coarse-domained and nanodomained materials. (a) Conventional diffraction of twin-related coarse domains, where fundamental Bragg peaks of constituent crystal split by vector $\Delta \mathbf{K}^{(1)}$ due to twinning shear and broaden due to finite size. Scattered waves from individual twin domains form reflection peaks (red and green filled with yellow) independently without interference. (b) Adaptive diffraction of nanotwins, where scattered waves from multiple nanodomains coherently superimpose to form new Bragg reflection peaks (blue filled with yellow), whose positions shift along the twin peak splitting vector $\Delta \mathbf{K}^{(1)}$ according to the twin variant volume fraction ω by following lever rule, while the conventional Bragg peaks (dashed red and green) disappear. The overlapping of broadened twin peaks is necessary to produce significant interference effects. Additional weak satellite peaks may arise from nanotwin superlattices. (c) When nanodomains coexist with coarse domains, the resultant peak profile (black filled with yellow) is an incoherent summation of the new adaptive peaks (blue) and the conventional peaks (red and green).

profile is illustrated in Fig. 1(c). Such extraordinary peak profile can easily be misinterpreted as evidence of a new phase coexisting with conventional phase.

(iv) *Superlattice Bragg reflection peaks*. For nanotwin superlattice, according to Eq. (2), the Bragg reflection peaks in reciprocal space are located at $\mathbf{k}^{(s)}=(K_x^{(1)}+\kappa^{(s)}, K_y^{(1)}, K_z^{(1)})$, which defines the reciprocal superlattice sites. According to $\kappa^{(s)}$ given in Eq. (4), these superlattice sites are distributed with equal distance $2\pi/T$ along the straight lines normal to twin plane and passing $\mathbf{K}^{(1)}$ along $\Delta \mathbf{K}^{(1)}$, i.e., the superlattice site distribution, twin peak splitting, and peak broadening are all along the same lines. It is worth noting that, in general, the superlattice sites $\mathbf{k}^{(s)}$ do not coincide with the fundamental peaks $\mathbf{K}^{(1)}$ or their twin peaks; in other words, the values $\kappa^{(s)}$ given in Eq. (4) cannot be reduced to 0 coinciding with $\mathbf{K}^{(1)}$ or $-\gamma \mathbf{s} \cdot \mathbf{K}^{(1)}$ coinciding with $\mathbf{K}^{(1)}+\Delta \mathbf{K}^{(1)}$. As a result, the fundamental reflection peaks of the constituent crystal will disappear, and new reflection peaks will appear at some reciprocal superlattice sites $\mathbf{k}^{(s)}$, whose visibility depends on their intensities that are determined by Eq. (3). The positions of $\mathbf{k}^{(s)}$ relative to $\mathbf{K}^{(1)}$ are determined by both the twin domain thickness and twin variant volume fraction. Consequently, fundamental peaks shift, split, disappear, and new

peaks appear, which of these phenomena occur and are observed depend on the twin domain thicknesses, twin variant volume fractions, variations of thicknesses and volume fractions in imperfect nanotwin superlattices, as well as instrumental resolutions; and the lattice parameters measured from the observed Bragg peaks at $\mathbf{k}^{(s)}$ are different from that of the constituent crystal. This is a pronounced peculiar diffraction behavior of nanotwins, which can be erroneously linked to new phases that do not exist if interpreted by conventional diffraction theory of coarse domains.

(v) *Coherent diffraction condition*. The condition for coherent diffraction of twin-related domains is closely related to the above-discussed phenomena of (i) twin peak splitting and (ii) peak broadening. It is worth noting that the twin peak splitting and peak broadening are along the same lines normal to twin planes. With the thickness of twin layers decreased to nanoscale, the twin peaks significantly broaden and eventually overlap, as illustrated by the dashed lines in Fig. 1(b). The overlapping of broadened twin peaks is a necessary condition for coherent scattering to produce significant effects through constructive (in-phase) and destructive (out-of-phase) interferences. For twin peaks to overlap, it requires small twin peak splitting (small twinning shear strain) and large peak broadening (small domain size). According to Eq. (6), the twin peak splitting distance is $\Delta K^{(1)} = \gamma |\mathbf{s} \cdot \mathbf{K}^{(1)}|$. According to $f_1(\kappa)$ and $f_2(\kappa)$ in Eq. (5), the half-width broadness of twin peaks are $2\pi/T_1$ and $2\pi/T_2$, respectively, as determined from the first zeros of the central maximum peaks described by $f_1(\kappa)$ and $f_2(\kappa)$. Therefore, the necessary condition for significant coherent diffraction effects of twin-related domains is

$$\gamma |\mathbf{s} \cdot \mathbf{K}^{(1)}| < 2\pi\left(\frac{1}{T_1} + \frac{1}{T_2}\right) = \frac{2\pi}{T}\left(\frac{1}{\omega} + \frac{1}{1-\omega}\right), \quad (7)$$

where $\omega = T_1/T$ is the twin variant volume fraction. For convenience, if we use $T_1 \approx T_2 \approx t$ as the typical twin domain thickness (i.e., $\omega=0.5$ corresponding to the minimum of the ω-dependent factor), Eq. (7) is simplified to

$$\gamma t |\mathbf{s} \cdot \mathbf{K}^{(1)}| < 4\pi. \quad (8)$$

It is noted that this condition is Brillouin zone dependent through $\mathbf{K}^{(1)}$. For high-index reflection spots $\mathbf{K}^{(1)}$ that yield large values of $\mathbf{s} \cdot \mathbf{K}^{(1)}$, the coherent diffraction condition is more stringent; thus conventional diffraction behaviors will be observed in high-order Brillouin zones where the coherent diffraction condition is not satisfied. In fact, peculiar nanotwin diffraction phenomenon can be observed only at those diffraction spots $\mathbf{K}^{(1)}$ with small $\mathbf{s} \cdot \mathbf{K}^{(1)}$ (usually with low index) and in materials with small twinning (ferroelastic) strain γ and nanoscale domain size t, so that Eq. (7) is satisfied. Note that *coherent diffraction* in this paper refers to the peculiar diffraction behaviors caused by coherent scattering and interference effects of multiple nanodomains, as compared to conventional diffraction behaviors of coarse domains. Coherent diffraction condition is given in Eq. (7). Under more stringent condition, coherent diffraction exhibits a pronounced special phenomenon that is well described by a *lever rule* according to twin variant volume fraction, which

we call *adaptive diffraction*, as discussed next.

(vi) *Adaptive diffraction condition*. There are m superlattice sites $\mathbf{k}^{(s)}$ distributed between neighboring fundamental peaks $\mathbf{K}^{(1)}$ along twin plane normal direction, where m is the number of atomic planes parallel to twin plane in the bilayer basis of nanotwin superlattice. However, not all of them are visible. In fact, only a few superlattice peaks $\mathbf{k}^{(s)}$ in the immediate vicinity of fundamental twin peaks could possibly gain observable intensities. The superlattice peak intensity is determined by $|g|^2$, where function $g(\kappa^{(s)}, \mathbf{K}^{(1)})$ is given in Eq. (3). In order to gain visible intensity, at least one of the two terms in $g(\kappa^{(s)}, \mathbf{K}^{(1)})$ must be nonzero. Therefore, only those $\mathbf{k}^{(s)}$ distributed within the broadened fundamental twin peaks are potentially visible. Since the full width broadness of twin peaks are $4\pi/T_1$ and $4\pi/T_2$, respectively, and the reciprocal superlattice site spacing is $2\pi/T$, only $2T/T_1$ and $2T/T_2$ superlattice peaks $\mathbf{k}^{(s)}$ are potentially observable around twin peaks, which could produce shifting and splitting of the fundamental twin peaks. For those $\mathbf{k}^{(s)}$ that are distributed inside the overlapped region of broadened twin peaks, their intensities depend on the interference between the broadened twin peaks and are determined by the cross product of the two complex terms in $g(\kappa^{(s)}, \mathbf{K}^{(1)})$, which would result in new peaks between the fundamental twin peaks. As has been shown for tetragonal nanotwins[1] and will be shown for rhombohedral nanotwins in Sec. III, when the superlattice site spacing is larger than the twin peak splitting distance, i.e.,

$$\gamma |\mathbf{s} \cdot \mathbf{K}^{(1)}| < \frac{2\pi}{T}, \qquad (9)$$

a single superlattice site $\mathbf{k}^{(s)}$ is located between twin peaks and gains strong intensity by constructive (in-phase) superposition, as illustrated in Fig. 1(b). The position of this observed new peak along $\Delta\mathbf{K}^{(1)}$ follows lever rule, i.e., the distance to the twin peaks is inversely proportional to the corresponding twin variant volume fraction, which produces the adaptive diffraction phenomenon. It is noted that Eq. (9) requires domain sizes at least four times smaller than that required by Eq. (7). Equation (9) is a sufficient condition for the special adaptive diffraction phenomenon of nanotwins, while Eq. (7) is the condition for general coherent diffraction effects. It is worth noting that, associated with nanotwin superlattice, additional satellite peaks may form at the nearby superlattice sites $\mathbf{k}^{(s)}$, as illustrated in Fig. 1(b), which, however, could be smeared out by the variations of thicknesses and volume fractions in imperfect superlattices and become very weak in intensity.

(vii) *Critical domain size*. Nanoscale domain sizes are required to observe coherent and adaptive diffraction phenomena. In the case of tetragonal (101) nanotwins previously analyzed,[1] using the coordinate system defined by unit vectors $\boldsymbol{\tau}$ (x axis) and $\mathbf{s}$ (z axis), the reciprocal lattice vector $\mathbf{K}^{(1)}$ with index (hkl) is $\mathbf{K}^{(1)} = 2\pi(h\cos\beta/a_t - l\sin\beta/c_t, k/a_t, h\sin\beta/a_t + l\cos\beta/c_t)$, where $\beta = \tan^{-1}(a_t/c_t)$. The twinning shear strain is $\gamma = 2\cot 2\beta$. The twin peak splitting distance is $\Delta K^{(1)} = 2\pi|h+l|(c_t^2 - a_t^2)/(c_t a_t \sqrt{c_t^2 + a_t^2})$. Note that there is no twin peak splitting

for (101) tetragonal twins if $h+l=0$. Substituting these values into Eq. (8) yields

$$\frac{t|h+l|}{2a_t} \frac{\varepsilon(2+\varepsilon)}{(1+\varepsilon)\sqrt{2+2\varepsilon+\varepsilon^2}} < 1, \qquad (10)$$

where $\varepsilon = (c_t - a_t)/a_t \approx \gamma/2$ is the tetragonality strain. Since $\varepsilon \ll 1$, Eq. (10) is simplified to

$$t\varepsilon|h+l| < \sqrt{2}a_t. \qquad (11)$$

As examples, for $h+l=1$ and $\varepsilon=0.01$, Eq. (11) requires twin domain thickness $t < 140a_t$; for $h+l=4$ and $\varepsilon=0.05$, it is drastically reduced to $t < 7a_t$. It shows that coherent diffraction effects could be observed in domains as large as hundreds of angstroms (tens of nanometers) at low-index reflection spots, and adaptive diffraction phenomenon requires smaller domain sizes (by a factor of 4 or more). It is noted that Eq. (7) is the condition required for coherent diffraction effects; in order to observe the effects, intensity condition must also be satisfied to produce visible modifications of the peak profiles, as determined by Eq. (3). Nevertheless, Eqs. (7)–(11) clearly show that coherent and adaptive diffraction effects are observed only at specific reflection spots ($h+l \sim 1$, usually with low index) in nanodomained materials ($t \sim 10$ nm) with small ferroelastic strain ($\varepsilon \sim 0.01$), and high-resolution x-ray and neutron diffraction techniques are required to resolve the fine peak structures. The same conclusion is reached for rhombohedral nanotwins, as will be presented in Sec. III.

(viii) *Brillouin zone dependence*. Coherent and adaptive diffractions produce markedly different peak profiles than conventional coarse-domain diffraction, as illustrated in Fig. 1. A transition between the different peak profiles can be observed in different Brillouin zones. For given nanodomain sizes, such a transition usually occurs between low-index and high-index reflection spots $\mathbf{K}^{(1)}$, because the conditions in Eqs. (7) and (9) are satisfied at low-index spots but not at high-index spots [accurately speaking, it is $\mathbf{s} \cdot \mathbf{K}^{(1)}$ that matters]. It is worth noting that such Brillouin zone-dependent fine peak structures are the signatures of nanotwins, and the transition provides quantitative information of nanodomain sizes. The Brillouin zone-dependent diffractions are critical experiments that distinguish heterogeneous nanotwins from homogeneous phases, which also allow determination of nanodomain sizes by diffraction measurements.

Adaptive diffraction behavior of tetragonal nanotwins has been previously analyzed with relevance to M_C phase.[1] In the following section, we apply the above-discussed diffraction theory to rhombohedral nanotwins, which has relevance to M_A and M_B phases.

III. APPLICATION TO RHOMBOHEDRAL NANOTWINS

Crystallographic analysis shows that rhombohedral domains can form two types of twin relations, namely, with {001} and {110} twin planes, respectively. The spontaneous ferroelastic lattice distortion with respect to cubic lattice is described by the following deformation matrix:

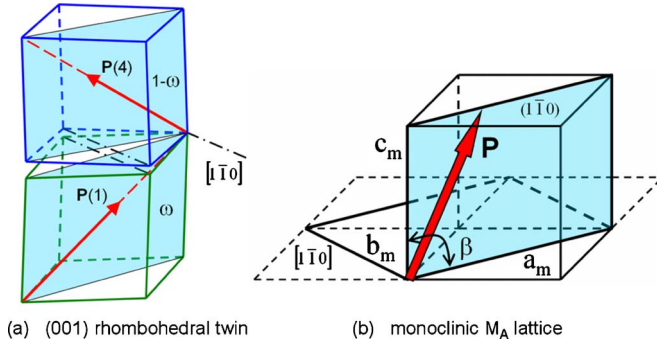(a) (001) rhombohedral twin   (b) monoclinic M_A lattice

FIG. 2. (Color online) Crystallographic illustrations of (001) rhombohedral twin and monoclinic M_A lattice. (a) Twin-related rhombohedral variants 1 and 4 with (001) twin plane, where the polarization vector in each variant is along [111] and [$\bar{1}\bar{1}$1], respectively, to form a head-to-tail pattern. The volume fractions of variants 1 and 4 are ω and 1-ω, respectively. The averaged polarization is confined to and rotates in (1$\bar{1}$0) symmetry plane. The averaged lattice has a monoclinic M_A symmetry. (b) The monoclinic M_A unit cell resulting from averaging (001) twin-related rhombohedral variants shown in (a). Note that the unique axis b_m is the common axis [1$\bar{1}$0] of rigid-body rotations of the twin variants 1 and 4 to close the gap between them.

$$\hat{\mathbf{A}} = \frac{a_r}{3a_c} \begin{bmatrix} \alpha_1 & \alpha_2 & \alpha_2 \\ \alpha_2 & \alpha_1 & \alpha_2 \\ \alpha_2 & \alpha_2 & \alpha_1 \end{bmatrix}, \tag{12}$$

where

$$\alpha_1 = \theta_1 + 2\theta_2, \quad \alpha_2 = \theta_1 - \theta_2, \tag{13}$$

$$\theta_1 = \sqrt{1 + 2\cos\alpha}, \quad \theta_2 = \sqrt{1 - \cos\alpha},$$

α is rhombohedral angle, and a_r and a_c are lattice parameters of rhombohedral and cubic phases, respectively. The value of a_c is usually extrapolated to the rhombohedral phase temperature; however, in the following derivation, the cubic lattice just serves as a reference state and the specific value a_c does not matter. The deformation matrix in Eq. (12) is for structural variant with rhombohedral axis along [111], indicated as variant 1 in Figs. 2 and 3. The deformation matrices for other three variants are obtained by applying cubic symmetry operations to $\hat{\mathbf{A}}$. In particular, for variant 4 with rhombohedral axis along $\pm[\bar{1}\bar{1}1]$ shown in Figs. 2 and 3, the deformation matrix with respect to cubic lattice is

$$\hat{\mathbf{A}}' = \frac{a_r}{3a_c} \begin{bmatrix} \alpha_1 & \alpha_2 & -\alpha_2 \\ \alpha_2 & \alpha_1 & -\alpha_2 \\ -\alpha_2 & -\alpha_2 & \alpha_1 \end{bmatrix}. \tag{14}$$

A. {001} nanotwin superlattice of rhombohedral phase

Figure 2(a) illustrates the crystallographic relationships of two rhombohedral variants with (001) twin plane. For convenience, we define the twin plane and twinning shear with respect to variant 1, i.e., variant 1 is fixed during twin for-

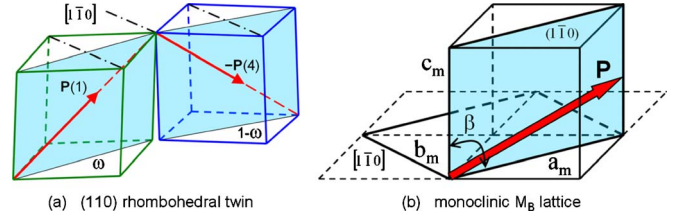(a) (110) rhombohedral twin   (b) monoclinic M_B lattice

FIG. 3. (Color online) Crystallographic illustrations of (110) rhombohedral twin and monoclinic M_B lattice. (a) Twin-related rhombohedral variants 1 and 4 with (110) twin plane, where the polarization vector in each variant is along [111] and [11$\bar{1}$], respectively, to form a head-to-tail pattern. The volume fractions of variants 1 and 4 are ω and 1-ω, respectively. The averaged polarization is confined to and rotates in (1$\bar{1}$0) symmetry plane. The averaged lattice has a monoclinic M_B symmetry. (b) The monoclinic M_B unit cell resulting from averaging (110) twin-related rhombohedral variants shown in (a). Note that the unique axis b_m is the common axis [1$\bar{1}$0] of rigid-body rotations of the twin variants 1 and 4 to close the gap between them.

mation and variant 4 rotates to close the gap angle between them. In the coordinate system associated with cubic lattice,

$$\boldsymbol{\tau} = \frac{1}{3\sqrt{1+\cos\alpha}} \begin{bmatrix} -\alpha_2 \\ -\alpha_2 \\ \alpha_1 + \alpha_2 \end{bmatrix}, \quad \mathbf{s} = \frac{\sqrt{2}}{6\sqrt{1+\cos\alpha}} \begin{bmatrix} -(\alpha_1 + \alpha_2) \\ -(\alpha_1 + \alpha_2) \\ -2\alpha_2 \end{bmatrix}. \tag{15}$$

The twinning shear strain is

$$\gamma = \frac{2\sqrt{2}\cos\alpha}{\theta_1\theta_2}. \tag{16}$$

The primitive superlattice translation vector is

$$\mathbf{L} = m_1\mathbf{l} + m_2\mathbf{l}', \quad \mathbf{l} = \frac{a_r}{3} \begin{bmatrix} \alpha_2 \\ \alpha_2 \\ \alpha_1 \end{bmatrix}, \tag{17}$$

$$\mathbf{l}' = \frac{a_r}{3(1+\cos\alpha)} \begin{bmatrix} (1-3\cos\alpha)\theta_1 - (1+3\cos\alpha)\theta_2 \\ (1-3\cos\alpha)\theta_1 - (1+3\cos\alpha)\theta_2 \\ (1-3\cos\alpha)\theta_1 + 2(1+3\cos\alpha)\theta_2 \end{bmatrix},$$

where m_1 and m_2 are the numbers of (001) atomic planes in respective twin layers of the bilayer basis, and $m = m_1 + m_2$. Using Eqs. (15) and (17) gives the layer thicknesses

$$T = \mathbf{L} \cdot \boldsymbol{\tau} = md, \quad T_1 = m_1 d, \quad T_2 = m_2 d, \tag{18}$$

$$d = a_r\theta_1\theta_2/\sqrt{1+\cos\alpha},$$

where d is the interplanar spacing of (001) atomic planes. The fundamental reciprocal lattice vector $\mathbf{K}^{(1)}$ with index (hkl) is

$$\mathbf{K}^{(1)} = \frac{2\pi}{3a_r\theta_1\theta_2} \begin{bmatrix} h\alpha_1 + (h-k-l)\alpha_2 \\ k\alpha_1 + (k-l-h)\alpha_2 \\ l\alpha_1 + (l-h-k)\alpha_2 \end{bmatrix}. \tag{19}$$

Equations (15), (16), and (19) give

$$\gamma \mathbf{s} \cdot \mathbf{K}^{(1)} = -\frac{4\pi(h+k)\cot\alpha}{a_r\theta_1}. \tag{20}$$

Substituting Eqs. (17)–(19) into Eq. (4) yields

$$\kappa^{(s)} = \frac{2\pi}{T}\left[s - lm + 2m_2(h+k)\frac{\cos\alpha}{1+\cos\alpha} \right]. \tag{21}$$

Using Eqs. (15)–(21) into Eq. (3) determines the superlattice peak intensities.

As discussed on Eqs. (7)–(11), coherent effects and adaptive diffraction phenomenon are observed in nanodomained materials with small ferroelastic strain. Using Eq. (20) into Eq. (7) gives the necessary condition for coherent diffraction

$$\frac{2|h+k|\cot\alpha}{a_r\theta_1} < \frac{1}{T_1} + \frac{1}{T_2}. \tag{22}$$

As its special form, Eq. (8) becomes

$$\frac{t|h+k|\cot\alpha}{a_r\sqrt{1+2\cos\alpha}} < 1. \tag{23}$$

Since $\alpha \approx 90°$, Eq. (23) is simplified to

$$t\cos\alpha|h+k| < a_r. \tag{24}$$

As examples, for $h+k=1$ and $\alpha=89.8°$, Eq. (24) requires twin domain thickness $t < 286a_r$; for $h+k=4$ and $\alpha=89.0°$, it is drastically reduced to $t < 14a_r$. Note that there is no twin peak splitting for (001) rhombohedral twins if $h+k=0$.

Small ferroelastic lattice distortion implies that the twin peak splitting distance $\Delta K^{(1)}$ is very small, thus $\tilde{n}_2^0(\mathbf{K}^{(1)} + \Delta\mathbf{K}^{(1)}) \approx \tilde{n}_2^0(\mathbf{K}^{(1)})$. For pseudocubic systems, such as the ferroelectric perovskites, $\tilde{n}_2^0(\mathbf{K}^{(1)}) \approx \tilde{n}_1^0(\mathbf{K}^{(1)})$ due to the cubic symmetry of crystal unit cell. Under these conditions, Eq. (3) shows that the superlattice peak intensities are proportional to $|\Psi|^2$, where the complex function Ψ is

$$\psi(s) = \frac{2}{\kappa_1}\sin\varphi_1 e^{i\varphi_1} + \frac{2}{\kappa_2}\sin\varphi_2 e^{-i\varphi_2}, \tag{25}$$

where

$$\kappa_1 = \kappa^{(s)}, \quad \varphi_1 = \frac{\kappa_1 T_1}{2}, \quad \kappa_2 = \kappa^{(s)} + \gamma\mathbf{s}\cdot\mathbf{K}^{(1)}, \quad \varphi_2 = \frac{\kappa_2 T_2}{2}. \tag{26}$$

Using Eqs. (18), (20), (21), and (26), it gives the relative phase angle between the two terms in Eq. (25) as

$$\Delta\varphi = \varphi_1 + \varphi_2 = \pi(s - lm). \tag{27}$$

We denote $s_0 = lm$. It is ready to show that

$$\mathbf{k}^{(s_0)} = \mathbf{K}^{(1)} + (1-\omega)\Delta\mathbf{K}^{(1)}, \tag{28}$$

where $\omega = m_1/m$ is the volume fraction of variant 1. Equations (27) and (28) show that the superlattice reflection peak

corresponding to $s = s_0$ undergoes in-phase ($\Delta\varphi=0$) constructive interference and gain high intensity, and its position along $\Delta\mathbf{K}^{(1)}$ follows a lever rule. Under condition of Eq. (7), new Bragg peak will appear at $\mathbf{k}^{(s_0)}$; under condition of Eq. (9), this peak will be the single strong peak appearing between the fundamental twin peaks, while the conventional twin peaks will disappear because they are off the superlattice sites. Since the nearest-neighbor superlattice sites correspond to $s = s_0 \pm 1$, they undergo out-of-phase ($\Delta\varphi = \pm\pi$) destructive interference and gain low intensity, which could be smeared out by instrumental resolution and variations of m_1 and m_2 in nanotwin superlattices. The superlattice peaks further away from $\mathbf{k}^{(s_0)}$ are also further off the broadened twin peaks and have diminishing intensities. Therefore, under adaptive diffraction condition of Eq. (9), the superlattice reflection peak at $\mathbf{k}^{(s_0)}$ has the highest intensity and is the one observed in experiment. It is noteworthy that the position of this new peak at $\mathbf{k}^{(s_0)}$, according to Eq. (28), is determined by a lever rule along the twin peak splitting vector $\Delta\mathbf{K}^{(1)}$, i.e., it adaptively shifts along $\Delta\mathbf{K}^{(1)}$ according to the twin variant volume fraction ω. This gives the adaptive diffraction phenomenon of nanotwins. It is also worth noting that the lattice parameters and lattice symmetry measured from this adaptive reflection peak $\mathbf{k}^{(s_0)}$ are different from that of the constituent crystal. A conventional interpretation of diffraction data will misinterpret the experimental results.

To derive the lattice parameters from the adaptive reflection peak $\mathbf{k}^{(s_0)}$, we consider several characteristic reflection spots usually used in experiments.[8] The lattice parameters measured from $\mathbf{k}^{(s_0)}$ around fundamental spots $\mathbf{K}^{(1)}$ with indices $(HH0)$, $(H\bar{H}0)$, and $(00L)$, respectively, are

$$a_m = \frac{a_r\sqrt{2(1+\cos\alpha)}}{\sqrt{1+2(2\omega-1)^2\cos^2\alpha/(\theta_1\theta_2)^2}} \approx \sqrt{2}a_r\sqrt{1+\cos\alpha},$$

$$b_m = \sqrt{2}a_r\sqrt{1-\cos\alpha}, \quad c_m = \frac{a_r\theta_1\theta_2}{\sqrt{1+\cos\alpha}} \approx a_r, \tag{29}$$

which correspond to a monoclinic M_A lattice, as illustrated in Fig. 2(b). It is noted that $(H\bar{H}0)$ and $(00L)$ spots do not undergo twin peak splitting ($h+k=0$) where $\mathbf{k}^{(s_0)}$ coincides with $\mathbf{K}^{(1)}$, thus the lattice parameters b_m and c_m determined from them do not depend on twin variant volume fraction ω. It is also noted that adaptive peak $\mathbf{k}^{(s_0)}$ appears at $(HH0)$ spot, but the lattice parameter a_m determined from it only has an insignificant dependence on ω.

The crystallographic analysis of (001) rhombohedral nanotwins by nanodomain averaging gives the same monoclinic M_A phase as concluded from above diffraction analysis. The deformation matrix averaged over twin domains is

$$\langle\hat{\mathbf{A}}\rangle = \omega\hat{\mathbf{A}} + (1-\omega)\mathbf{R}\hat{\mathbf{A}}', \tag{30}$$

where

$$R_{ij} = \delta_{ij}\cos 2\phi + n_i n_j(1-\cos 2\phi) - e_{ijk}n_k\sin 2\phi \tag{31}$$

is the rigid-body rotation matrix of the twin variant 4 with respect to variant 1, where δ_{ij} is Kronecker delta and e_{ijk} is permutation symbol. The relative rigid-body rotation closes

the gap angle between the twin-related variants that is caused by the ferroelastic lattice distortion, retaining the lattice coherency between twinned crystals. The gap (rigid-body rotation) angle is 2ϕ, as illustrated in Fig. 2(a), where

$$\phi = \tan^{-1} \frac{\sqrt{2}\alpha_2}{\alpha_1 + \alpha_2} \approx \frac{\sqrt{2}}{2} \cos \alpha. \tag{32}$$

The rigid-body rotation axis **n** is

$$\mathbf{n} = (\boldsymbol{\tau} \times \mathbf{s})/|\boldsymbol{\tau} \times \mathbf{s}|, \tag{33}$$

which is parallel to $(1,-1,0)$. Since the two twin variants undergo relative rigid-body rotation about the common $[1\bar{1}0]$ axis, as highlighted by the dash-dotted lines in Fig. 2(a), the $[1\bar{1}0]$ axis is not affected by such a relative rigid-body rotation and defines a unique b_m axis for the M_A unit cell, as shown in Fig. 2(b). The lattice parameter b_m is not affected by the nanotwin averaging and is identical to that of rhombohedral lattice measured along $[1\bar{1}0]$, which gives the same b_m as in Eq. (29). The rigid-body rotation also gives rise to the perceived monoclinic angle β. The averaged deformation matrix in Eq. (30) defines the Cauchy (linear and infinitesimal) strain

$$\varepsilon_{ij} = \frac{1}{2}(\langle A_{ij}\rangle + \langle A_{ji}\rangle) - \delta_{ij}, \tag{34}$$

whose normal strain components along $[110]$, $[1\bar{1}0]$, and $[001]$, respectively, give the monoclinic lattice parameters

$$a_m \approx \sqrt{2}a_r\left(1 + \frac{1}{2}\cos\alpha\right), \quad b_m = \sqrt{2}a_r\sqrt{1 - \cos\alpha}, \quad c_m \approx a_r, \tag{35}$$

which are equivalent to the relations in Eq. (29) given the smallness of $\cos \alpha$ (i.e., $\alpha \approx 90°$).

For the (001) rhombohedral twin of variants 1 and 4 illustrated in Fig. 2(a), the polarization is $\mathbf{P}(1) = P_R/\sqrt{3}(1,1,1)$ in variant 1 and is $\mathbf{P}(4) = P_R/\sqrt{3}(-1,-1,1)$ in variant 4, which form a head-to-tail pattern to eliminate domain wall charge and minimize electrostatic energy. The polarization averaged over the twin-related variants is

$$\mathbf{P} = \mathbf{P}(1)\omega + \mathbf{P}(4)(1 - \omega) = \frac{P_R}{\sqrt{3}}(2\omega - 1, 2\omega - 1, 1), \tag{36}$$

which is confined to the symmetry plane $(1\bar{1}0)$, as highlighted by the shaded planes in Fig. 2. When the twin variant volume fraction ω is changed by external electric field or applied stress through domain wall movement, the averaged polarization **P** rotates continuously in $(1\bar{1}0)$ plane, as experimentally observed in monoclinic M_A phase. The b_m axis, i.e., $[1\bar{1}0]$, is normal to the symmetry plane $(1\bar{1}0)$ of continuous rotation of averaged polarization.

B. {110} nanotwin superlattice of rhombohedral phase

Figure 3(a) illustrates the crystallographic relationships of two rhombohedral variants with (110) twin plane. As in the case of (001) rhombohedral twin, we define the twin plane and twinning shear with respect to variant 1, and variant 4 rotates to close the gap angle between them. We follow the same procedure of derivation in Sec. III A, and only present results for (110) twin that are different from (001) twin.

In the coordinate system associated with cubic lattice,

$$\boldsymbol{\tau} = \frac{1}{3\sqrt{2}}\begin{bmatrix} \alpha_1 \\ \alpha_1 \\ -2\alpha_2 \end{bmatrix}, \quad \mathbf{s} = -\frac{1}{3}\begin{bmatrix} \alpha_2 \\ \alpha_2 \\ \alpha_1 \end{bmatrix}. \tag{37}$$

The twinning shear strain is the same as in Eq. (16). The primitive superlattice translation vector is

$$\mathbf{L} = m_1\mathbf{l} + m_2\mathbf{l}', \tag{38}$$

$$\mathbf{l} = \frac{a_r}{3}\begin{bmatrix} \alpha_1 \\ \alpha_2 \\ \alpha_2 \end{bmatrix},$$

$$\mathbf{l}' = \frac{a_r}{3}\begin{bmatrix} (1 - 2\cos\alpha)(\theta_1 - \theta_2) \\ (1 - 2\cos\alpha)\theta_1 + 2(1 + \cos\alpha)\theta_2 \\ (1 - 2\cos\alpha)\theta_1 - (1 + 4\cos\alpha)\theta_2 \end{bmatrix},$$

where m_1 and m_2 are the numbers of (110) atomic planes in respective twin layers of the bilayer basis. Using Eqs. (37) and (38) gives the layer thicknesses

$$T = \mathbf{L} \cdot \boldsymbol{\tau} = md, \quad T_1 = m_1d, \quad T_2 = m_2d, \quad d = a_r\theta_1\theta_2/\sqrt{2}, \tag{39}$$

where d is the interplanar spacing of (110) atomic planes. The fundamental reciprocal lattice vector $\mathbf{K}^{(1)}$ with index (hkl) is the same as in Eq. (19). Equations (16), (19), and (37) give

$$\gamma\mathbf{s} \cdot \mathbf{K}^{(1)} = -\frac{4\sqrt{2}\pi l \cos\alpha}{a_r\theta_1\theta_2}. \tag{40}$$

Substituting Eqs. (19), (38), and (39) into Eq. (4) yields

$$\kappa^{(s)} = \frac{2\pi}{T}(s - hm_1 - km_2 + 2lm_2\cos\alpha). \tag{41}$$

Using Eqs. (16), (19), and (37)–(41) into Eq. (3) determines the superlattice peak intensities.

Using Eq. (40) into Eq. (7) gives the necessary condition for coherent diffraction

$$\frac{2\sqrt{2}|l|\cos\alpha}{a_r\theta_1\theta_2} < \frac{1}{T_1} + \frac{1}{T_2}. \tag{42}$$

As its special form, Eq. (8) becomes

$$\frac{\sqrt{2}t|l|\cos\alpha}{a_r\sqrt{(1 + 2\cos\alpha)(1 - \cos\alpha)}} < 1, \tag{43}$$

which, given $\alpha \approx 90°$, is simplified to

$$t\cos\alpha|l| < a_r/\sqrt{2}. \tag{44}$$

As examples, for $l=1$ and $\alpha=89.8°$, Eq. (44) requires twin domain thickness $t < 202a_r$; for $l=4$ and $\alpha=89.0°$, it is dras-

tically reduced to $t < 10a_r$. Note that there is no twin peak splitting for (110) rhombohedral twins if $l=0$.

Small ferroelastic lattice distortion and pseudocubic symmetry of crystal unit cell imply that $\tilde{n}_1^0(\mathbf{K}^{(1)}) \approx \tilde{n}_2^0(\mathbf{K}^{(1)} + \Delta\mathbf{K}^{(1)})$. The superlattice peak intensities are proportional to $|\Psi|^2$, where Ψ is defined in Eqs. (25) and (26). Using Eqs. (39)–(41) into Eq. (26) gives the relative phase angle between the two terms in Eq. (25) as

$$\Delta\varphi = \varphi_1 + \varphi_2 = \pi(s - hm_1 - km_2). \tag{45}$$

We denote $s_0 = hm_1 + km_2$. It is readily shown that Eq. (28) and the lever rule hold for (110) nanotwins. Therefore, adaptive diffraction phenomenon is observed for (110) rhombohedral nanotwin superlattice. The discussion on (001) rhombohedral nanotwin superlattice in Sec. III A following Eq. (28) also applies to (110) nanotwins.

To derive the lattice parameters from the adaptive reflection peak $\mathbf{k}^{(s_0)}$, we also consider characteristic $(HH0)$, $(H\bar{H}0)$, and $(00L)$ fundamental reflection spots $\mathbf{K}^{(1)}$ usually used in experiments.[8] The lattice parameters measured from $\mathbf{k}^{(s_0)}$ around these respective spots are

$$a_m = a_r\sqrt{2(1 + 2\cos\alpha)(1 - \cos\alpha)} \approx \sqrt{2}a_r\sqrt{1 + \cos\alpha},$$

$$b_m = \sqrt{2}a_r\sqrt{1 - \cos\alpha},$$

$$c_m = \frac{a_r}{\sqrt{1 + 2(2\omega - 1)^2\cos^2\alpha/(\theta_1\theta_2)^2}} \approx a_r, \tag{46}$$

which correspond to a monoclinic M_B lattice, as illustrated in Fig. 3(b). It is noted that $(HH0)$ and $(H\bar{H}0)$ spots do not undergo twin peak splitting ($l=0$) where $\mathbf{k}^{(s_0)}$ coincides with $\mathbf{K}^{(1)}$, thus the lattice parameters a_m and b_m determined from them do not depend on twin variant volume fraction ω. It is also noted that adaptive peak $\mathbf{k}^{(s_0)}$ appears at $(00L)$ spot, but the lattice parameter c_m determined from it only has an insignificant dependence on ω.

The crystallographic analysis of (110) rhombohedral nanotwins by nanodomain averaging gives the same monoclinic M_B phase as concluded from above diffraction analysis. The deformation matrix averaged over twin domains is also defined by Eqs. (30) and (31). The gap (rigid-body rotation) angle is 2ϕ, as illustrated in Fig. 3(a), where

$$\phi = \tan^{-1}\frac{\sqrt{2}\alpha_2}{\alpha_1} \approx \frac{\sqrt{2}}{2}\cos\alpha, \tag{47}$$

which is different from but practically equal to that for (001) twin given in Eq. (32) because of $\alpha \approx 90°$. The rigid-body rotation axis $\mathbf{n}$ is defined by Eq. (33) with $\boldsymbol{\tau}$ and $\mathbf{s}$ given in Eq. (37), which is again parallel to $(1,-1,0)$. Since the two twin variants undergo relative rigid-body rotation about the common $[1\bar{1}0]$ axis, as highlighted by the dash-dotted lines in Fig. 3(a), the $[1\bar{1}0]$ axis is not affected by such a relative rigid-body rotation and defines a unique b_m axis for the M_B unit cell, as shown in Fig. 3(b). The lattice parameter b_m is not affected by the nanotwin averaging and is identical to that of rhombohedral lattice measured along $[1\bar{1}0]$, which

gives the same b_m as in Eq. (46). The rigid-body rotation also gives rise to the perceived monoclinic angle β. The Cauchy strain is defined in Eq. (34) in terms of the averaged deformation matrix given in Eq. (30), whose normal strain components along $[110]$, $[1\bar{1}0]$, and $[001]$, respectively, give the same monoclinic lattice parameters as in Eq. (35), which are equivalent to the relations in Eq. (46) given the smallness of $\cos\alpha$ ($\alpha \approx 90°$).

It is worth noting that the lattice parameters of M_A and M_B phases are practically the same given the smallness of $\cos\alpha$ (i.e., $\alpha \approx 90°$), as given in Eqs. (29) and (46), respectively. The difference between M_A and M_B crystal lattices lies in the orientation of polarization in ferroelectric states. For the (110) rhombohedral twin of variants 1 and 4 illustrated in Fig. 3(a), the polarization is $\mathbf{P}(1) = P_R/\sqrt{3}(1,1,1)$ in variant 1 and is $\mathbf{P}(4) = P_R/\sqrt{3}(1,1,-1)$ in variant 4 to form a head-to-tail pattern. The polarization averaged over the twin-related variants is

$$\mathbf{P} = \mathbf{P}(1)\omega + \mathbf{P}(4)(1 - \omega) = \frac{P_R}{\sqrt{3}}(1, 1, 2\omega - 1), \tag{48}$$

which is confined to the symmetry plane $(1\bar{1}0)$, as highlighted by the shaded planes in Fig. 3. When the twin variant volume fraction ω is changed through domain wall movement, the averaged polarization $\mathbf{P}$ rotates continuously in $(1\bar{1}0)$ plane, as experimentally observed in monoclinic M_B phase. The b_m axis, i.e., $[1\bar{1}0]$, is normal to the symmetry plane $(1\bar{1}0)$ of continuous rotation of averaged polarization. It is noted that the averaged polarization is along $(2\omega - 1, 2\omega - 1, 1)$ in M_A [Eq. (36)] while is along $(1, 1, 2\omega - 1)$ in M_B [Eq. (48)]. Since the variant volume fraction is in the range of $0 < \omega < 1$, the absolute values of the polarization components satisfy $P_X = P_Y < P_Z$ in M_A while $P_X = P_Y > P_Z$ in M_B.

IV. DISCUSSIONS

The general behaviors of coherent and adaptive diffractions of twin-related nanodomains and, in particular, nanotwin superlattices are described by Eqs. (2)–(9) and are discussed in Sec. II in comparison to conventional diffraction phenomena of coarse domains. Equation (7) gives the necessary condition for observation of coherent scattering and interference effects; Eq. (9) gives the sufficient condition for adaptive diffraction phenomenon. It is shown that coherent and adaptive diffraction phenomena are observed only at specific (usually low-index) fundamental reflection spots in nanodomained materials with small ferroelastic lattice distortions, which require high-resolution x-ray and neutron diffraction techniques to resolve the fine structures of peak profiles. This could be one of the reasons that monoclinic phases mimicked by nanotwins in ferroelectric perovskite solid solutions were not observed until recently in high-resolution synchrotron x-ray diffraction experiment.[6]

One important signature of nanotwin diffraction is the Brillouin zone dependence of fine peak structures. This dependence is due to the dependence of the coherent and adap-

tive diffraction conditions, i.e., Eqs. (7) and (9), on the fundamental reflection spots $\mathbf{K}^{(1)}$. For given nanodomain sizes, such conditions are satisfied in some Brillouin zones usually corresponding to low-index reflection spots, and adaptive reflection peaks are observed at these spots; while in other Brillouin zones usually corresponding to high-index reflection spots, such conditions are not satisfied and conventional twin peaks are observed. It is worth noting that previous experiments only examined low-index spots, such as (H00) and (HH0) with $H=2$.[5] In order to observe the Brillouin zone-dependent diffraction behaviors, it is required to examine higher-index reflection spots, say, with larger values of H. The fine structures of peak profiles and the transition from adaptive diffraction to conventional diffraction in terms of the reflection index (hkl) not only unambiguously reveal the heterogeneous nature of nanotwins, but also quantitatively determine the feature sizes of nanodomains in the diffraction samples.

The transition from conventional diffraction to adaptive diffraction also occurs if domain sizes change from coarse domains to nanodomains. For given reflection spot $\mathbf{K}^{(1)}$, the critical domain size of such a transition is determined by Eq. (9). It is worth noting that the domain sizes could change drastically instead of gradually from micrometer scale to nanometer scale, in response to the change in electric field, temperature, or composition. As observed by TEM in PMN-PT[4] and PZT,[7] nanometer-sized domains form inside micrometer-sized domains, which together form hierarchical domain microstructures. It is not necessary for coarse domains to gradually evolve and miniaturize into nanodomains; instead, nanodomains may directly form inside coarse domains, converting coarse domains into higher-level structural hierarchy. Associated with such sudden change in the lowest-level domain sizes without going through the intermediate domain size range defined by the conditions in Eqs. (7) and (9), a drastic transition from conventional peak profile to adaptive peak profile is observed, without exhibiting the intermediate coherent diffraction effects. This transition will be perceived by diffraction in the same manner of phase transition, as observed in MPB-based ferroelectrics between rhombohedral, tetragonal, and monoclinic phases.[5]

To make analytical formulation tractable, nanotwin superlattices are considered in deriving Eqs. (2)–(5). Nanotwin superlattices are reasonable approximation of the nanodomain microstructures in real materials. Ferroelastic domains self-assemble into twin-related microstructures, i.e., polytwins, to accommodate spontaneous lattice distortion and minimize elastic energy.[9,10] Since the dimension of coherent scattering volume is of the order of coherent length of diffraction radiation and is much larger than the nanotwin thickness, nanoscale polytwins can be idealized as nanotwin superlattices. Coherence effect in the scattering from a pair of twin nanodomains of equal thickness has also been discussed recently, which demonstrates significant modification of peak intensity profile;[11] however, the results of such a single-pair nanodomain configuration do not directly apply to real nanodomained, polytwinned materials. It is worth noting that, even Eq. (28) is obtained for perfect nanotwin superlattices, the adaptive diffraction phenomenon and the lever rule of adaptive peak position are also valid for imperfect

nanotwin superlattices, i.e., with variations in twin layer thickness and variant volume fraction. Since the adaptive peak at $\mathbf{k}^{(s_0)}$ only depends on twin variant volume fraction but is not sensitive to twin layer thickness as long as condition in Eq. (9) is satisfied, variation in twin layer thickness has little effect on the position and intensity of the adaptive peak. However, according to Eq. (4), the positions of other superlattice reflection peaks strongly depend on the layer thickness $T=T_1+T_2$, and variations in T_1 and T_2 drastically smear out these peaks and make satellite peaks very weak. On the other hand, the position of the adaptive peak is determined by the twin variant volume fraction ω according to lever rule, thus variation in ω could broaden and weaken the adaptive peak; however, variation in ω is relatively small since the twin variant volume fraction is determined by the strain-accommodation requirement, i.e., invariant plane strain condition,[9,10] which defines the value of ω on a length scale of nanotwin thickness to minimize the volume-dependent strain energy. Consequently, the adaptive diffraction is a pronounced phenomenon observable in imperfect nanotwin superlattices or nanoscale polytwins; that is, the adaptive peak always appears at well-defined position exhibiting strong intensity whenever adaptive diffraction condition of Eq. (9) is satisfied. This fact is in agreement with the widely reported diffraction observations of monoclinic phases in MPB-based ferroelectrics,[5] where nanotwins mimic monoclinic phases through adaptive diffraction behavior.

The adaptive diffraction phenomenon of nanodomains is drastically different from that of coarse domains, where a conventional interpretation of the diffraction data would link the new adaptive peaks to new phases that do not exist. In the cases of tetragonal and rhombohedral nanotwins, conventional interpretation of adaptive diffraction phenomenon leads to identification of monoclinic phases. However, these monoclinic phases are not independent new phases but intrinsically related to the constituent phases of nanotwins. The signature of such intrinsic relationships is revealed quantitatively in their lattice parameters. In particular, three intrinsic lattice parameter relationships have been shown to exist between M_C and tetragonal phases over wide ranges of electric field, temperature, and composition in PMN-PT and PZN-PT.[2] These quantitative relationships can be derived by either adaptive diffraction theory[1] or crystallographic analysis[2,3] of tetragonal nanotwins, which both give the same results. In Sec. III of this paper, the general diffraction theory of nanotwin superlattices is applied to the cases of two types of rhombohedral nanotwins, and three intrinsic lattice parameter relationships are shown to exist between M_A and M_B and rhombohedral phases; and crystallographic analysis gives the same results.

For both (001) and (110) rhombohedral nanotwins, given $\alpha\approx90°$, the relationships in Eqs. (29) and (46) are

$$\frac{a_m}{\sqrt{2}}\approx a_r\left(1+\frac{1}{2}\cos\alpha\right),\quad \frac{b_m}{\sqrt{2}}\approx a_r\left(1-\frac{1}{2}\cos\alpha\right),\quad c_m\approx a_r,$$

$$(49)$$

from which we can rewrite the three intrinsic lattice parameter relationships between rhombohedral and both monoclinic M_A and M_B phases as
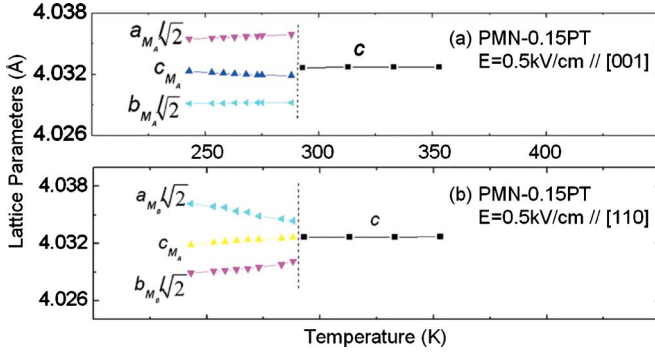
FIG. 4. (Color online) Single-crystal x-ray diffraction measurement of monoclinic phase lattice parameters of PMN-15%PT in field cooling (reproduced with permission—Ref. 8). (a) M_A phase observed in field cooling with 0.5 kV/cm along [001] axis. (b) M_B phase observed in field cooling with 0.5 kV/cm along [110] axis.

$$\frac{1}{2}\left(\frac{a_m}{\sqrt{2}} + \frac{b_m}{\sqrt{2}}\right) = a_r, \qquad (50a)$$

$$c_m = a_r, \qquad (50b)$$

$$\alpha = \cos^{-1}\frac{a_m - b_m}{\sqrt{2}c_m}. \qquad (50c)$$

We examine these relationships against experimental data. Figure 4 shows the lattice parameters of monoclinic M_A and M_B phases measured by single-crystal x-ray diffraction of PMN-15%PT in field cooling experiments.[8] The composition of PMN-15%PT is off the MPB ($\sim 30\%$PT), and rhombohedral phase is observed without electric field. With the application of electric field of magnitude 0.5 kV/cm, different monoclinic phases are observed depending on the direction of the electric field: M_A in [001] field and M_B in [110] field. The experimental lattice parameters are used in Eqs. (50a)–(50c) to examine the three lattice parameter relationships, as shown in Fig. 5. The lattice parameter a_r is calculated using Eq. (50a) and is plotted as open circles ($\bigcirc$) in Figs. 5(a) and 5(b), which, according to Eq. (50b), is equal to c_m. This relationship is fulfilled over the entire experimental temperature range, where the agreement is within 0.001 Å comparable to experimental accuracy. The rhombohedral angle α is calculated using Eq. (50c) and is plotted in Fig. 5(c), which shows agreement between the cases of M_A and M_B phases. The calculated a_r and α are in good agreement with the experimental a_r and α shown as solid diamonds ($\blacklozenge$) in Fig. 5, which are obtained by extrapolating the room-temperature x-ray powder diffraction data[12] of rhombohedral PMN-26%PT and PMN-20%PT to PMN-15%PT (the field cooling experiments of PMN-15%PT[8] did not report experimental values of a_r and α).

Adaptive diffraction phenomenon is observed at fundamental reflection spots of constituent crystals that undergo twin peak splitting. For the spots with index (hkl) that do not exhibit twin peak splitting, i.e., $\mathbf{s}\cdot\mathbf{K}^{(1)}=0$ according to Eq. (6), such as $h+k=0$ for (001) rhombohedral twin, $l=0$ for (110) rhombohedral twin, and $h+l=0$ for (101) tetragonal
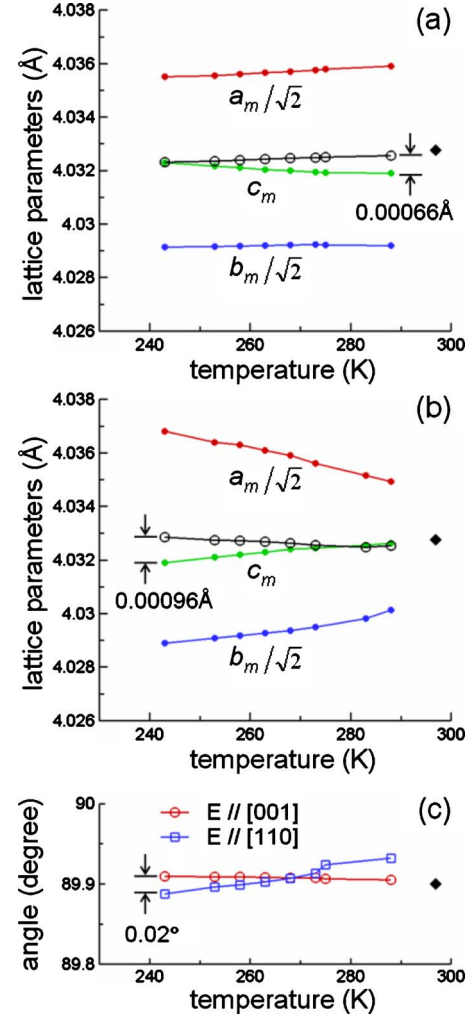

FIG. 5. (Color online) Three intrinsic lattice parameter relationships between the intermediate monoclinic phases and conventional rhombohedral phase of PMN-15%PT in field cooling. The first and second relationships are shown for (a) M_A and (b) M_B phases, where data of solid circles are taken from experiments (Ref. 8) (Fig. 4), and data of open circles are calculated from Eq. (50a). The third relationship is shown in (c), where data are calculated from Eq. (50c). The data of solid diamonds are for rhombohedral phase obtained from experiment (Ref. 12).

twin, Eq. (4) gives $\kappa^{(s_0)}=0$, and Eq. (28) gives $\mathbf{k}^{(s_0)}=\mathbf{K}^{(1)}$. That is, the adaptive reflection peaks coincide with the fundamental reflection peaks, thus no new peak is observed. These reflection peaks are not affected by nanotwins and give lattice parameters that are exactly equal to that measured from the corresponding fundamental peaks of the constituent crystals (i.e., coarse domains), such as b_m and c_m in Eq. (29) measured from $(H\bar{H}0)$ and $(00L)$ spots, a_m and b_m in Eq. (46) measured from $(HH0)$ and $(H\bar{H}0)$ spots, and b_m in Eq. (1) measured from $(0K0)$ spot.

As shown in this paper for rhombohedral nanotwins and in previous papers[1–3] for tetragonal nanotwins, both diffraction analysis and crystallographic analysis give the same lattice parameter relationships. However, crystallographic analysis does not provide more information except the aver-

age lattices on a length scale of coherence length. In order to investigate nanodomain sizes, reflection peak intensity profiles and, in particular, the Brillouin-zone-dependent diffraction behaviors, diffraction analysis is required.

Finally, it is worth noting that, when adaptive diffraction condition in Eq. (9) is satisfied and diffraction perceives nanotwins as a new phase, the atomic structural parameters extracted from the diffraction peak profiles, e.g., by Rietveld refinement technique, do not have a physical basis, since such a new phase does not exist. This has been demonstrated recently for PZT.[7] Clearly, it is an important issue to incorporate the coherent scattering and interference effects into Rietveld refinement through some parameters reflecting nanodomain sizes and twin configurations, which is a topic of our further investigation.

V. SUMMARY

Nanotwins exhibit Brillouin-zone-dependent diffraction behaviors. When adaptive diffraction condition, Eq. (9), is satisfied, new Bragg reflection peak appears between conventional twin peaks and adaptively shifts along twin peak splitting vector, whose position is determined by lever rule according to twin variant volume fraction. The new adaptive reflection peaks correspond to "new" phases with symmetry and lattice parameters different from but intrinsically related to that of the constituent crystals of nanotwins. In particular, rhombohedral nanotwins of {001} and {110} twin planes mimic monoclinic M_A and M_B phases, respectively, and tetragonal nanotwins of {101} twin plane mimic M_C phase. Intrinsic lattice parameter relationships exist between the perceived monoclinic phases and the constituent phases of nanotwins. Similar adaptive diffraction phenomena should occur in other nanodomained materials, such as piezoelectric, magnetostrictive, and ferroelastic/martensitic materials. Therefore, the coherent scattering and interference effects must be taken into account in diffraction data interpretation and phase identification for nanodomained materials.

---

*yuwang@mse.vt.edu

[1] Y. U. Wang, Phys. Rev. B **74**, 104109 (2006).

[2] Y. U. Wang, Phys. Rev. B **73**, 014113 (2006).

[3] Y. M. Jin, Y. U. Wang, A. G. Khachaturyan, J. F. Li, and D. Viehland, Phys. Rev. Lett. **91**, 197601 (2003); J. Appl. Phys. **94**, 3629 (2003).

[4] H. Wang, J. Zhu, N. Lu, A. A. Bokov, Z. G. Ye, and X. W. Zhang, Appl. Phys. Lett. **89**, 042908 (2006).

[5] For complete references to the monoclinic phases, see recent review: B. Noheda and D. E. Cox, Phase Transitions **79**, 5 (2006).

[6] B. Noheda, D. E. Cox, G. Shirane, J. A. Gonzalo, L. E. Cross, and S. E. Park, Appl. Phys. Lett. **74**, 2059 (1999).

[7] K. A. Schönau, L. A. Schmitt, M. Knapp, H. Fuess, R. A. Eichel, H. Kungl, and M. J. Hoffmann, Phys. Rev. B **75**, 184117 (2007).

[8] H. Cao, J. Li, D. Viehland, and G. Xu, Phys. Rev. B **73**, 184110 (2006).

[9] A. G. Khachaturyan, *Theory of Structural Transformations in Solids* (Wiley, New York, 1983).

[10] A. L. Roytburd, J. Phys. IV **C8**, 21 (1995).

[11] H. Boysen, J. Phys.: Condens. Matter **19**, 275206 (2007).

[12] A. K. Singh and D. Pandey, Phys. Rev. B **67**, 064102 (2003).